 doi:10.20944/preprints202208.0271.v1

Article

A Non-enzymatic Electrochemical Sensor of Cu@Co-MOF Composite for Glucose Detection with High Sensitivity and Selectivity

Zhen-Zhen Ma [1], Bing Liu [2], Huang Jiao [1,*] and Ling Xu [1,*]

[1] Key Laboratory of Macromolecular Science of Shaanxi Province, Shaanxi Key Laboratory for Advanced Energy Devices, Shaanxi Engineering Laboratory for Advanced Energy Technology, School of Chemistry & Chemical Engineering, Shaanxi Normal University, Xi'an 710062, Shaanxi Province, P. R. China
[2] College of Chemistry and Chemical Engineering, Shaanxi Key Laboratory of Chemical Additives for Industry, Shaanxi University of Science and Technology, Xi'an 710021, Shaanxi Province, P. R. China
* Correspondence: xuling@snnu.edu.cn (L. Xu); huangjiao@snnu.edu.cn (H. Jiao)

Abstract: The integration of metal nanoparticles and solid carriers can achieve ideal stability, high load and good conductivity. In this work, copper nanoparticles (Cu NPs) were sequentially deposited on a cobalt metal-organic framework (Co-MOF) by bonding with exposed imino groups, followed by a reduction reaction to prepare a new Cu@Co-MOF composite. Cu@Co-MOF acts as a non-enzymatic electrochemical sensor to detect glucose (Glu) in an alkaline medium. The composite working electrode of Cu@Co-MOF/GCE (GCE = glassy carbon electrode) improves the electrocatalytic activity for Glu oxidation. Cu@Co-MOF/GCE shows excellent electrocatalytic performances in Glu concentration ranging 0.005~1.8 mmol·L^{-1} (mM): the sensitivities are 282.89 μA·mM^{-1}·cm^{-2} in 0.005-0.4 mM Glu and 113.15 μA·mM^{-1}·cm^{-2} in 0.4-1.8 mM Glu respectively with low detection limit of 1.6 μM (S/N = 3) and high selectivity and stability.

Keywords: non-enzymatic sensor; glucose; cobalt metal-organic framework; electrochemical detection

1. Introduction

As the most important monosaccharide, glucose (Glu) plays a crucial role in the body function. Glu provides the main energy source of the body, which hydrolyzes in the body and is stored as glycogen. Glu can protect and detoxify the liver, and also promotes the metabolism of poisons. Glu is the most important and basic substance in medicine. It can be adsorbed fast by human tissues [1]. However, the fluctuation of blood Glu hazards the health. For example, hypoglycemia leads to brain dysfunction, induces cardiovascular diseases of arrhythmia, myocardial infarction and stroke, and causes nervous diseases; hyperglycemia will result in dehydration, metabolic dysfunction, water electrolyte disorder, fatigue, decreased resistance, especially, diabetes. Diabetes is a main predisposition to other serious illnesses of kidney failure, stroke, and blindness, causing a huge financial burden [2]. Thus, an accurate, low-cost, and easy measurement method for sensing Glu in human body is in a great need [3,4]. The measurement methods of Glu mainly include chromatography, spectroscopy and electrochemistry [5,6]. The electrochemical Glu sensors have the advantages of high reliability, low-cost and outstanding operability, which attract a lot of interest [7,8]. Electrochemical Glu sensors are divided into enzymatic and non-enzymatic sensors. The enzymatic Glu sensors occupy the main part in the market of Glu sensor industry, but the enzymatic Glu sensors show enzyme activity-depending sensitivities [9]. Their detection performances are seriously influenced by some environmental factors such as room temperature, humidity, pH value, etc [10]. Some limitations are related with enzyme such as enzyme payload, enzyme activity, poor reproducibility and

Preprints (www.preprints.org) | NOT PEER-REVIEWED | Posted: 16 August 2022 doi:10.20944/preprints202208.0271.v1

poor stability during process [11]. Totally, enzyme has become a difficulty to some degree in the development and application of enzymatic Glu sensors.

Compared with enzymatic Glu sensors, non-enzymatic sensors are easy to realize long-term and stable Glu detection, whose detection performances are not influenced by environmental factors, providing a support for high-performance continuous monitoring of Glu. Non-enzymatic Glu sensors have much more choices in material platforms to achieve larger surface area rather than the stacking of enzymes. For example, metal-organic frameworks (MOFs) are a kind of porous materials constructed by the self-assembly of metal ions with organic ligands into highly ordered structures [12,13]. Their poor conductivity blocks raw MOFs as Glu sensing electrocatalysts. Metal nanoparticles (NPs), such as nano gold and silver, have high specific surface areas, catalytic activity and electrical conductivity. Doping metal NPs into the electrochemical Glu sensors can greatly improve the conductivities and the detection performances of the MOF-based electrochemical Glu sensors [14,15]. Furthermore, MOFs and metal NPs integrate into modified electrodes as Glu sensors with the effective reaction areas and the interface electron migration rates. It shows the advantages of high catalysis and high sensitivity for the oxidation of Glu. Without limitations in biological enzymes, the working electrodes of NPs@MOFs composites are of great significance as non-enzymatic Glu sensors with high sensitivities and anti-interference [16,17]. Due to the high cost of nano novel metal-based electrochemical sensors, the application of nano transition metals in electrochemical sensors is expected to reduce the cost but not to sacrifice the advantages of doping nano novel metal. The preparation and large-scale application of low-cost and high-performance transition metal-based electrochemical devices are a support for Glu detection [18,19].

Our work presents a cobalt MOF (Co-MOFs), $[Co_3(BDC)_3(DMU)_2]$, as a non-enzymatic Glu sensor, which was prepared under ionothermal conditions. The Co-MOF was characterized in detail by single crystal X-ray diffraction (SCXRD), powder X-ray diffraction (XRD), Fourier transform infrared spectroscopy (FT-IR), thermogravimetric analysis (TGA), energy dispersive X-ray spectrometry (EDS) and X-ray photoelectron spectroscopy (XPS). Cu@Co-MOF and its composite electrode Cu@Co-MOF/GCE (GCE = glassy carbon electrode) were prepared through a sequential deposition-reduction process. Cu@Co-MOF/GCE electrode exhibits a high electrocatalytic performance to Glu detection, which returns accurate Glu concentrations in human serum and orange juice. Cu@Co-MOF/GCE can be regarded as a non-enzymatic electrochemical Glu sensor with high sensitivity, anti-interference, reproducibility, stability and rapid current response.

2. Materials and Methods

2.1. Materials and instruments

All chemicals are in analytical grade and pursued from commercial sources without purification. $Co(NO_3)_2{\cdot}6H_2O$, $CuSO_4$, terephthalic acid (H_2BDC), ethanol, methanol, N,N-dimethylformamide (DMF), $NaBH_4$, Al_2O_3 (0.5 μm and 50 nm) powder, HNO_3, H_2SO_4, KCl, $K_3Fe(CN)_6$ NaOH, Glu were bought from Sinopharm Chemical. (Shanghai, China). Interferents of D-Mannose (D-Man), D-fructose (D-Fru), aspartic acid (AA), dopamine (DA) urea and uric acid (UA) were got from Aladdin (Shanghai, China). Choline chloride (ChCl) and 1,3-dimethylurea (DMU) were purchased from Tokyo Chemical (Japan). Nafion solution of 5 wt% was bought from Sigma-Aldrich (Shanghai, China). KBr pellets of FT-IR grade was bought from Aldrich. Minutemaid orange juice was bought from a local supermarket.

XRD were measured on a Rigaku MiniFlex 600 (Japan) diffractometer under 40 kV and 15 mA at room temperature. FT-IR spectra were collected on a Bruker Tensor 27 FT-IR spectrometer in the wave number range of 4000–400 cm^{-1}. TGA was performed on a SDT Q600 V8.3 Build 101 instrument with a heating rate of 10 °C·min^{-1} and in a N_2 atmosphere with a flow rate of 20 $cm^3{\cdot}min^{-1}$. The surface elemental contents were determined by EDS on a Philips–FEI Quanta 200 scanning electron microscope. XPS was used to investigate the chemical states of the surface elements in Co-MOF on an Axis Ultra (Kratos

Preprints (www.preprints.org) | NOT PEER-REVIEWED | Posted: 16 August 2022 doi:10.20944/preprints202208.0271.v1

Analytical Ltd., UK). A CHI 660E (Shanghai, CH Instruments, Inc.) electrochemical workstation from CH Instruments, Inc (Shanghai, China) inspected all electrochemical measurements at room temperature.

2.2. Preparation

Co-MOF. $Co(NO_3)_2 \cdot 6H_2O$ (0.40 mmol, 0.1164 g) and H_2BDC (0.20 mmol, 0.0332 g) were mixed with a deep eutectic solvent (DES)-type ionic liquid of ChCl (1 mmol, 0.1396 g) and DMU (2 mmol, 0.1762 g) as in a crystallisation vial. The mixture was heated at 100 °C for 3 days, and naturally cooled to room temperature. The as-synthesized purple crystals of Co-MOF were washed with DMF and ethanol, and collected for the further characterizations. FT-IR data (in KBr, cm^{-1}): 3475(w), 3411(m), 3352(m), 2927(w), 2370(w), 2073(w), 1595(s), 1388(s), 1142(w), 1013(m), 886(m), 822(s), 748(s), 543(s).

Cu^{2+}/Co-MOF. Three groups of *ca*. 0.1238 g Co-MOF were added into 4 mL $CuSO_4$ methanol solution with concentrations of 5, 10, and 15 $mmol \cdot L^{-1}$ (mM) respectively. After 6 h continuous stirring, the suspensions were centrifuged and dried in a vacuum oven at 60 ºC for 12 h to obtain Cu^{2+}@Co-MOF.

Cu@Co-MOF. Three groups of 10, 20, and 30 mg $NaBH_4$ were dissolved in 4 mL methanol, and then mixed with the above Cu^{2+}/Co-MOF with a 30 min strong agitation. The mixture turned to black immediately, the suspensions were filtered, washed with methanol and dried at 60 ºC to obtain Cu@Co-MOF.

Cu@Co-MOF/GCE electrode. 0.5 μm and 50 nm alumina slurry on a polishing cloth were continuously used to polish a GCE with a 5-mm diameter to a mirror surface, then washed with HNO_3 solution of V_{water}:V_{HNO3} = 1:1, anhydrous ethanol and ultrapure water by sonication. GCE was further activated by 0.5 M H_2SO_4 and 0.1 M KCl/5 mM $K_3Fe(CN)_6$ respectively. 5 mg ground Cu@Co-MOF powder was dispersed in 1 mL anhydrous ethanol with 20 min sonication to form a uniform Cu@Co-MOF suspension of 5 $mg \cdot mL^{-1}$. Cu@Co-MOF/GCE electrode was obtained by a 10-μL Cu@Co-MOF suspension and a 5-μL nafion solution of 5 wt% was dropped on the GCE surface, then dried at room temperature.

2.3. Electrochemical measurements

Three-electrode system was used in the electrochemical measurements: the as-prepared Cu@Co-MOF/GCE is as the working electrode, a platinum wire as the counter electrode and KCl saturated Ag/AgCl as the reference electrode. The electrochemical performance of Cu@Co-MOF/GCE for sensing Glu was estimated by cyclic voltammetry (CV) and amperometric *I-t* curve methods.

2.4. Crystal structure determination

A suitable single crystal was mounted and collected the crystal data on a Bruker D8 Quest CCD diffractometer with a Cu-Kα radiation with λ = 1.54184 Å at 120 K. The crystal data was reduced via the ω scan technique by Bruker XSCANS program, and the direct method was used to solve the crystal structure of Co-MOF with SHELXL-2014/7 crystallographic software package. All non-hydrogen atoms were refined anisotropically. The positions of all hydrogen atoms were calculated according to their carriers, then were isotropically in the final refinement stage.

Crystal data (excluding structure factors) of Co-MOF has been deposited in the Cambridge Crystallographic Data Centre (CCDC) with No. of 2195853. The data can be obtained free from CCDC via www.ccdc.cam.ac.uk/data_request/cif.

3. Results

3.1. Structure description

$[Co_3(BDC)_3(DMU)_2]$ (Co-MOF) crystalizes in the triclinic *P*ī space group, whose asymmetric unit contains one and a half Co(II) centers, three separated BDC^{2-} ligands of 0.5 occupancy and a DMU molecule. BDC^{2-} ligand adopts two coordination modes of μ_4-

Preprints (www.preprints.org) | NOT PEER-REVIEWED | Posted: 16 August 2022 doi:10.20944/preprints202208.0271.v1

bis-bidentate bridging and μ4-bis-monodentate bridging/chelating (Supplementary information (SI), Figure S1). Six-coordinated Co1 locates in an octahedron constructed by six carboxylate oxygen atoms from six separated BDC^{2-} ligands. Five-coordinated Co2 is in a square pyramidal geometry, in which four carboxylate oxygen atoms from two BDC^{2-} ligands shape the basal plane, and an oxygen from DMU is in the apex. Central Co2 connects two symmetric terminal Co1 by two pairs of μ2-bidentate COO^- groups and one pair of μ2-monodentate bridging/chelating COO^- groups respectively, and one DMU ligand binds to each terminal Co1 into a linear trinuclear $[Co_3(COO)_6(DMU)_2]$ secondary building unit (SBU) (SI, Figure S2). Neighboring $[Co_3(COO)_6(DMU)_2]$ SBUs are connected by the three separated BDC^{2-} ligands with O11/O12 and O31/O32 (μ4-bis-bidentate bridging), or O21/O22 (μ4-bis-monodentate bridging/chelating) into three 1D chains along the [110], [011] and *b*-directions respectively (SI, Figure S3a-c). The chains along the [110] and *b*-directions weave a 2D layer, which topologizes a [4,4] network. The 2D layers further stack into a 3D framework with the fabrication of the chains along the [011] direction [Figure 1]. With the rest phenyl rings of the three separated BDC^{2-} ligands dummied as the 2-connected sticks and the $[Co_3(COO)_6(DMU)_2]$ SBUs as the six-connected nodes, the point symbols of the rest phenyl rings are {8}, and the one of $[Co_3(COO)_6(DMU)_2]$ is $\{8^{12}.12^3\}$. Therefore, the 3D framework is topologized as a 2,6-connected $\{8^{12}.12^3\}\{8\}_3$ network.

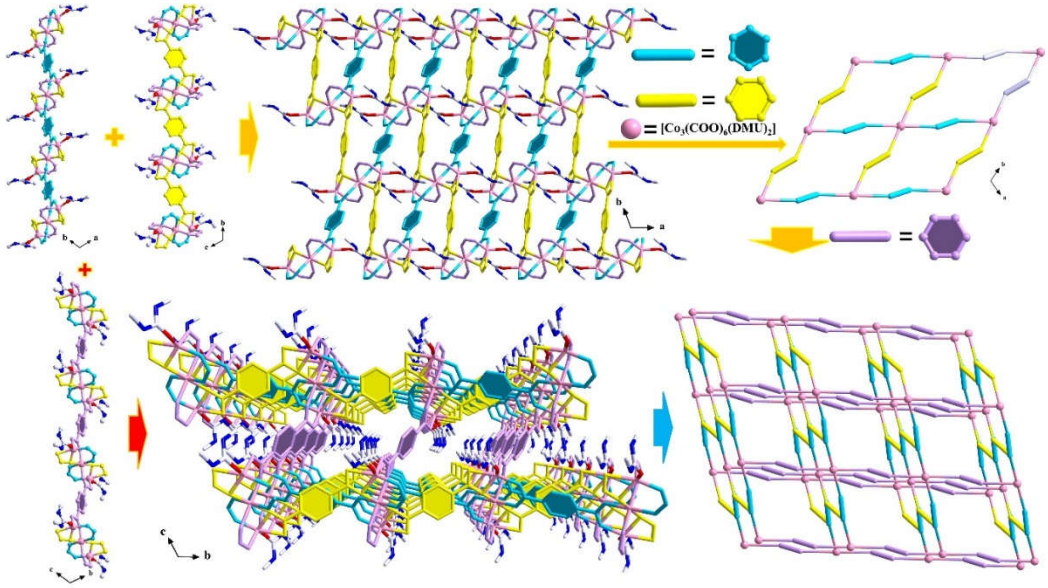

Figure 1. The structure construction of Co-MOF.

3.2. Characterizations

XRD. The experimental and simulated XRD patterns of Co-MOF, and those of Co-MOF and Cu@Co-MOF were compared (SI, Figure S4). The experimental XRD pattern of Co-MOF is in good agreement with the one simulated from the single crystal data, indicating that the bulk sample of Co-MOF is in high crystallinity and purity for the following characterizations. In the synthetical process of Cu@Co-MOF, metal precursors contained in organic solvents were used, a part of which will deposit on the surface of Co-MOF after drying, and then tend to aggregate into nanosheets. While, high concentration $NaBH_4$ solution reduces Cu^{2+}, thus to avoid Cu NPs unevenly aggregating on the surface of Co-MOF [20]. The XRD diffraction peaks of Co-MOF can be easily identified from those of Cu@Co-MOFs, indicating that Co-MOF stays the structural stability after Cu NPs are loaded. Comparing all Cu@Co-MOFs with Cu^{2+} ranging 5, 10, and 15 mM, the same XRD patterns demonstrate the isomorphism and the independence of Co-MOF on Cu^{2+} concentrations.

FT-IR. The characteristic absorption peaks of Co-MOF, Cu@Co-MOF and free H_2BDC ligand are analyzed by FT-IR (SI, Figure S5). The peaks within 3410−3310 cm^{-1} and 1650-

Preprints (www.preprints.org) | NOT PEER-REVIEWED | Posted: 16 August 2022 doi:10.20944/preprints202208.0271.v1

1550 cm^{-1} are related with the symmetric and asymmetric stretching vibration peaks of −NH from the secondary amine DMU in Co-MOF and Cu@Co-MOF, which don't appear in H_2BDC. Those in 3100-3000 cm^{-1} are attributed to very weak $\upsilon_{C\text{-}H}$ from phenyl rings in Co-MOF, Cu@Co-MOF and H_2BDC. Compared to 1682 cm^{-1} of carbonyl in free H_2BDC, the peaks respectively move to 1720-1550 cm^{-1} and 1450-1250 cm^{-1}, attributed to the asymmetric and symmetric stretching vibrations ($\upsilon_{as(\text{-}COO)}$ and $\upsilon_{s(\text{-}COO)}$) of the carboxyl groups in Co-MOF and Cu@Co-MOF. The wavelength differences are larger than 200 cm^{-1}, supporting the carboxyl groups are in coordination [21,22], agreeing with the structural analysis. Comparing Cu@Co-MOF with Co-MOF, the peaks at 3348 and 3388 cm^{-1} become weak, concerning with the interactions between Cu NPs and −NH groups after Cu^{2+} deposing-reducing on Cu-MOF; similarly, the peaks at 1552 and 1626 cm^{-1} are weakened, but the one at 1594 cm^{-1} concerning with the in-plane bending vibration of −NH groups. All changes support that Cu^{2+} loads on Co-MOF through the interaction between Cu^{2+} and −NH groups during the composite process [23,24].

TGA. The TGA curve shows there are three steps in the thermal decomposition of Co-MOF (Figure S6). There is a weight loss of only *ca.* 1.85% before 340 °C, coming from the loss of absorbed water or organic solvents. The second weigh loss of 20.68% is contributed to the removal of DMU as the temperature rises to 400 °C, very close to the calculated value of 20.85%. Followed with the collapse of the MOF skeleton, the third decomposition ends at 570 °C with 44.75 % weight loss, relating with the decomposition of BDC^{2-} ligands.

EDS. Surface elemental contents of Co-MOF and Cu@Co-MOF were analyzed by EDS. C, N, O and Co elements can be observed on the surface of Co-MOF with the contents of 65.10, 7.47, 21.57 and 5.85 at% respectively (Figure S7a), basically in accord with the formula $C_{30}H_{28}Co_3N_4O_{14}$. Besides C, N, O, and Co elements with closed contents (64.10, 6.13, 25.23, and 4.40 at% for C, N, O, and Co respectively) in Cu@Co-MOF, there is Cu element of 0.22 at%, demonstrating the load of Cu NPs on the surface of Co-MOF (Figure S7b).

XPS. Surface electronic states and the compositions of Co-MOF and Cu@Co-MOF were inspected by XPS. XPS of Co 2p in Co-MOF, Cu^{2+}/Co-MOF and Cu@Co-MOF are listed in Figure 2, which mainly includes Co $2p_{3/2}$ and Co $2p_{1/2}$ characteristic regions. The Co $2p_{3/2}$ region in Co-MOF contains the main peak at 781.29 eV and the accompanying one at 786.22 eV (Figure 2a). Similarly, the main peak at 797.15 eV and its accompanying peak at 802.70 eV can be found in the Co $2p_{1/2}$ region in Co-MOF; in Cu^{2+}/Co-MOF, the main and accompanying peaks in Co $2p_{3/2}$ region are at 781.48 and 786.13 eV respectively, those in Co $2p_{1/2}$ region are at 797.32 and 802.60 eV (Figure 2b); the corresponding main and accompanying peaks of Cu@Co-MOF are at 781.59 and 786.20 eV in Co $2p_{3/2}$ region, and at 797.39 and 802.69 eV in Co $2p_{1/2}$ region, respectively (Figure 2c). By comparing the above peaks, Co-MOF, Cu^{2+}/Co-MOF and Cu@Co-MOF show the same main and the accompanying peaks both in Co $2p_{3/2}$ and Co $2p_{1/2}$ characteristic regions, indicating the incorporation with Cu^{2+} or Cu NPs doesn't change the valence state of Co(II) cation.

XPS of Cu $2p_{3/2}$ and Cu $2p_{1/2}$ characteristic regions in Cu^{2+}/Co-MOF and Cu@Co-MOF are also compared (Figure 3). In Cu^{2+}/Co-MOF, the peaks at 933.26 eV in Cu $2p_{3/2}$ and at 953.78 eV in Cu $2p_{1/2}$ correspond to Cu(II) (Figure 3a). Differently, there exists four peaks in Cu $2p_{3/2}$ and Cu $2p_{1/2}$ regions of Cu@Co-MOF: those at 932.80 eV in Cu $2p_{3/2}$ and 952.55 eV in Cu $2p_{1/2}$ are contributed to Cu(0); those are at 935.27 eV in Cu $2p_{3/2}$ and 954.82 eV in Cu $2p_{1/2}$ related with Cu(II) (Figure 3b) [25,26,27]. It indicates that Cu^{2+} deposits on the surface of Co-MOF to form Cu^{2+}/Co-MOF, but only a part of deposited Cu^{2+} were reduced to Cu(0). Cu^{2+} and Cu(0) co-exist on the surface of Cu@Co-MOF.

Preprints (www.preprints.org) | NOT PEER-REVIEWED | Posted: 16 August 2022 doi:10.20944/preprints202208.0271.v1

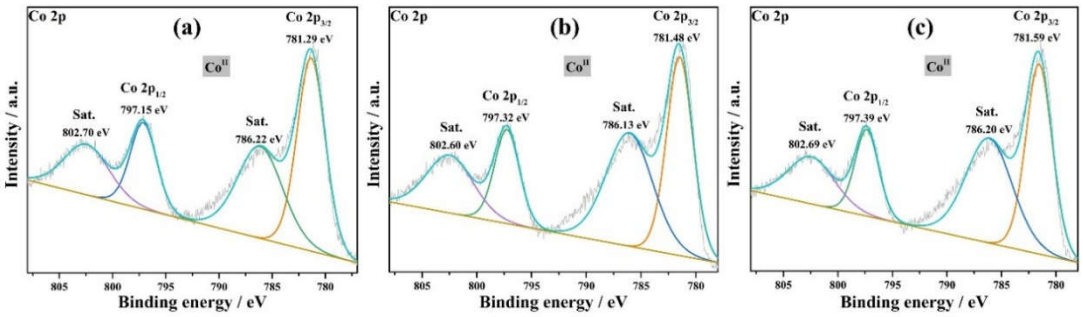

Figure 2. XPS of Co 2p in (a) Co-MOF, (b) Cu^{2+}/Co-MOF and (c) Cu@Co-MOF.

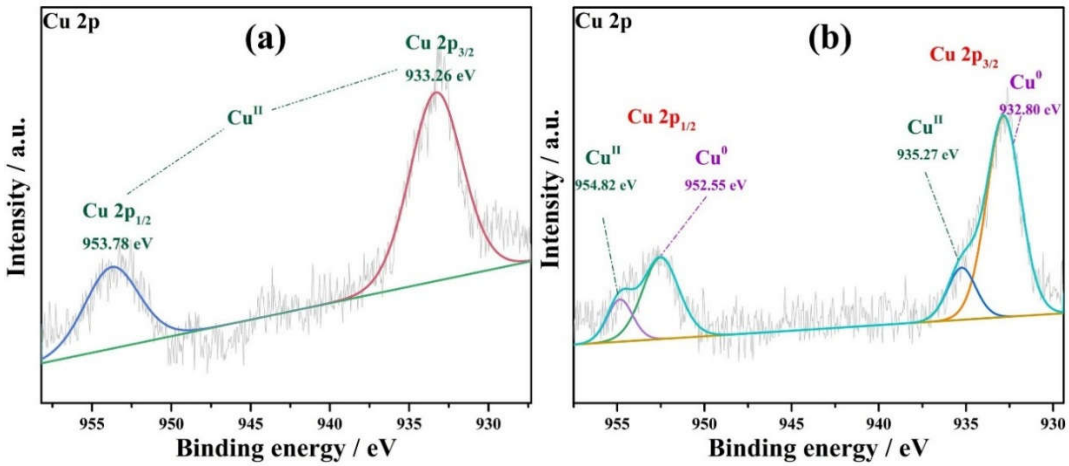

Figure 3. XPS of Cu 2p in (a) Cu^{2+}/Co-MOF and (b) Cu@Co-MOF.

3.3. Electrochemically sensing Glu by non-enzymatic Cu@Co-MOF

CV test. Cu@Co-MOF was modified on the surface of GCE to prepare Cu@Co-MOF/GCE as a working electrode. CV tests were carried out in 0.01 M NaOH at a working potential of +0.6 V (Figure 4). The redox peaks of Co^{II}/Co^{III} can be obviously observed in all the CV curves of Cu@Co-MOF with feeding Cu^{2+} concentrations (C_{Cu2+}) within 5-15 mM. With C_{Cu2+} increasing, the redox peaks weaken, indicating C_{Cu2+} of 5 mM shows the most sensitive current response (Figure 4a). Therefore, 5 mM is selected as the feeding Cu^{2+} concentration for the subsequent tests. By comparing Cu@Co-MOF/GCE and Co-MOF/GCE in the potential *vs* current response, Cu@Co-MOF/GCE shows a much stronger redox peak, indicating the conductivity of Co-MOF improved by Cu NPs. After 1 mM Glu is added, the redox peak of Co-MOF/GCE slightly weaken, suggesting an insensitivity of Co-MOF/GCE to Glu. Differently, Cu@Co-MOF/GCE causes the anode and cathode currents increased greatly at the initial potential of + 0.4 V as 1 mM Glu is added（Figure 4b）. It suggests that Cu@Co-MOF/GCE has a better catalytic oxidation effect on Glu with the improved conductivity. The mechanism of Co-MOF sensing Glu concerns a Glu oxidizing process explained by Reactions **1** and **2**. The XPS analysis of Co^{2+} before and after the electrocatalytic test supports this oxidation mechanism.

- Co^{II}-MOF + OH^- − e^- → Co^{III}-MOF (**1**)

  Co^{III}-MOF + glucose → Co^{II}-MOF + gluconolactone (**2**)

Preprints (www.preprints.org) | NOT PEER-REVIEWED | Posted: 16 August 2022 doi:10.20944/preprints202208.0271.v1

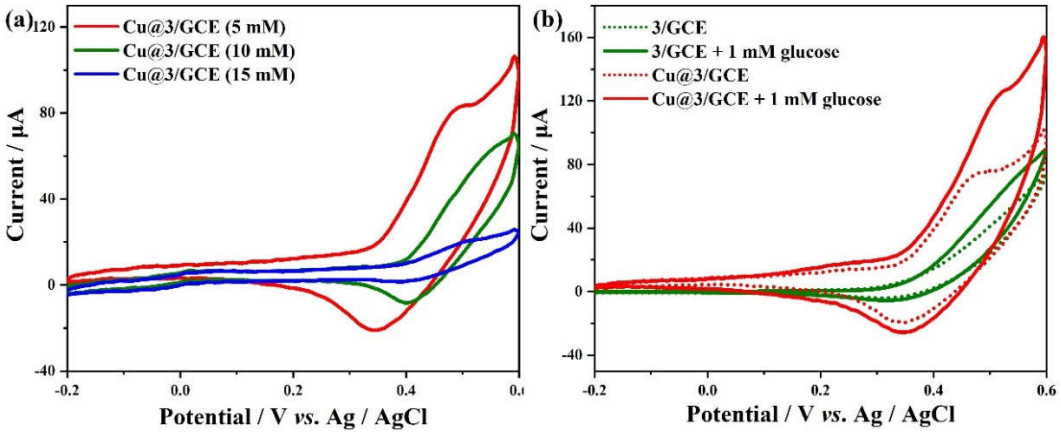

Figure 4. (a) CV curves of Cu@Co-MOF/GCE with Cu^{2+} concentration within 5-15 mM; (b) CV curves of Cu@Co-MOF/GCE and Co-MOF/GCE in 0.01 M NaOH with (solid line) or without (dash line) 1 mM Glu added.

Amperometric *I-t* curve test. The chronoamperometric response of Cu@Co-MOF/GCE to Glu concentrations (C_{Glu}) ranging 0.005-1.8 mM was recorded in 0.01 M NaOH at the working potential of +0.6 V. With Glu added, the current response gradually increases with increased C_{Glu} (Figure 5a). By depicting the plot of detected current *vs* C_{Glu}, the linear relationships can be figured out in the C_{Glu} sections of 0.005-0.4 mM and 0.4-1.8 mM. The linear equations are as follows with high correlation coefficient R^2:

C_{Glu} = 0.005-0.4 mM:

$$j_{Cu@Co-MOF/GCE}\ (mA\ cm^{-2}) = 0.020C_{Glu}(\mu M) + 8.266\ (R^2 = 0.9802)$$

C_{Glu} = 0.4-1.8 mM:

$$j_{Cu@Co-MOF/GCE}\ (mA\ cm^{-2}) = 0.012C_{Glu}(\mu M) + 6.096\ (R^2 = 0.9800)$$

EDS analysis shows only 0.22 at% Cu deposits on Co-MOF, meaning *ca.* one Cu corresponding to 30 Co^{II}. It hints a saturation effect in Cu@Co-MOF/GCE sensing Glu. It comes from the fact that all active sites of Cu NPs loading on Co-MOF are occupied by Glu molecules. The sensitivities of Cu@Co-MOF/GCE are calculated as 282.89 μA mM^{-1} cm^{-2} within C_{Glu} = 0.005-0.4 mM, and 113.15 μA mM^{-1} cm^{-2} within C_{Glu} = 0.4-1.8 mM. The detection limit was dived to 1.6 μM at a signal-to-noise (S/N) ratio of 3.

Cu@Co-MOF/GCE is compared with other reported non-enzymatic electrochemical Glu sensors in Table 1. Its detection limit of 1.6 μM is lower than a lot of non-enzymatic electrochemical Glu sensors, and comparable to Cu@HHNs (1.97 μM) [30], Au@Ni-BTC (1.5 μM) [37], CPO-27-Ni^{II} (1.46 μM) [38], and Co^{II}-MOF/Acb (1.7 μM) [47], but higher than Ni/Co(HHTP)MOF/CC (0.1 μM) [28], NiCo–LDH/CC (0.12 μM) [31], Co-MOF/EG (0.58 μM) [35], $Cu(OH)_2$@CoNi-LDH NT-NSs/GSPE (0.6 μM) [36], SiCNPs-ENFM (0.56 μM) [3], NiCo-MOF (0.29 μM) [40], UiO-67@Ni-MOF (0.98 μM) [41] and Ag@TiO_2@ZIF-67 (0.99 μM) [46]. Similarly, the sensitivity of 282.89 μA mM^{-1} cm^{-2} within C_{Glu} = 0.005-0.4 mM is more sensitive than most of the reported electrochemical Glu sensors, but lower than some sensors, such as Ni/Co(HHTP)MOF/CC (3250 μA mM^{-1} cm^{-2}) [28], CoZn-BTC/GCE (1218 μA mM^{-1} cm^{-2}) [19], Cu@HHNs (1594.2 μA mM^{-1} cm^{-2}) [30] and $Ni_{0.7}Co_{0.3}(OH)_2$ (1541 μA mM^{-1} cm^{-2}) [33]. Totally, Cu@Co-MOF/GCE shows a low detection limit and a high sensitivity to Glu electrochemical detection.

Preprints (www.preprints.org) | NOT PEER-REVIEWED | Posted: 16 August 2022 doi:10.20944/preprints202208.0271.v1

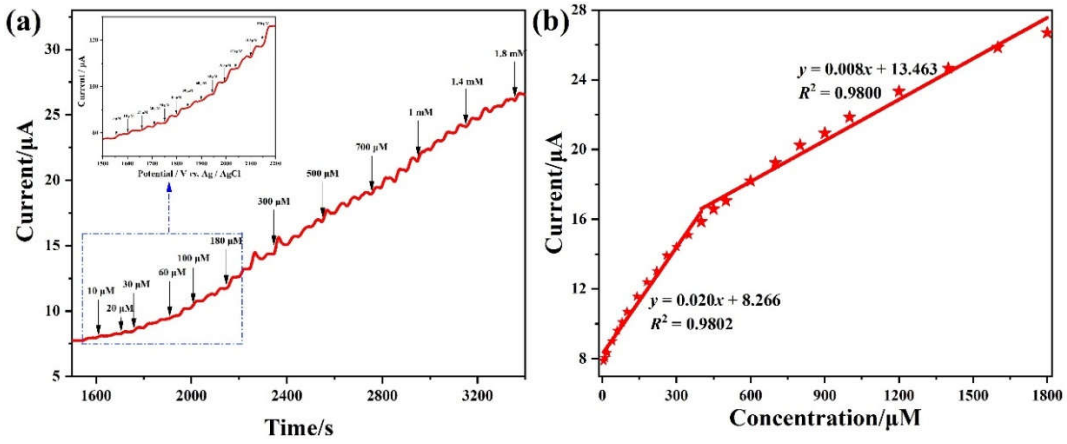

Figure 5. (a) The chronoamperometric curves of Cu@Co-MOF/GCE to C_{Glu} ranging 0.005-1.8 mM in 0.01 M NaOH at a working potential of +0.6 V; (b) the calibration curves of current *vs* C_{Glu}.

Table 1. Comparison of detection performances of reported non-enzymatic electrochemical Glu sensors with Cu@Co-MOF.

Electrodes	Detection limit (μM)	Detection range (mM)	Sensitivity (μA·mM^{-1}·cm^{-2})	Refs.
Cu@Co-MOF	1.6	0.005~0.4 0.4~1.8	282.89 113.15	This work
Ni/Co(HHTP)MOF/CC	0.1	0.3~2.312	3250	28
CoZn-BTC/GCE	4.7	0.001~0.255 0.255~2.53	1218 510	19
$Co_{0.33}Ni_{0.67}$-HLDH	3.1	0.01~2	242.9	29
Cu@HHNs	1.97	0.005~3	1594.2	30
NiCo–LDH/CC	0.12	0.001~1.5	5.12	31
Ni(TPA)-SWCNT	4.6	0.02~4.4	-	32
$Ni_{0.7}Co_{0.3}(OH)_2$	3.42	0.5~2.5	1541	33
CuTiPNPs	7	0.25~2	7.81	34
Co-MOF/EG	0.58	0.001~3.3	330	35
$Cu(OH)_2$@CoNi-LDH NTNSs/GSPE	0.6	0.002~3.2 3.2~7.7	1895 1322	36
Au@Ni-BTC	1.5	0.005~7.4	1447.1	37
CPO-27-Ni^{II}	1.46	0.04~6	40.95	38
SiCNPs-ENFM	0.56	0.5~20	30.75	3
Cu-in-ZIF-8/SPCE	2.76	0~0.7	412	17
Cu-Ni/NF	2	0.001~0.6	11340	39
MWCNTs-PB	4.95	0.01~1	105.93	18
NiCo-MOF	0.29	0.001~3.8	684.4	40
UiO-67@Ni-MOF	0.98	0.005~3.9	203.4	41
CoPO MA/NF	1	0.001~1.16	3.55	42
Cu_2O@ZIF-67	6.5	0.01~10 10~16.3	307.02 181.34	43
AgNPs/MOF-74	4.7	0.01~4	1.29	44

Preprints (www.preprints.org) | NOT PEER-REVIEWED | Posted: 16 August 2022 doi:10.20944/preprints202208.0271.v1

Ag@TiO_2@ZIF-67	0.99	0.048~1	78.8	45
Co^{II}-MOF/Acb	1.7	0.005~1	255	46
Cu-hemin MOFs	2.73	0.009~36	22.77	47
Tb@mesoMOFs-CNT	8	0.025~17	-	48
Co NP/Porous C	5.69	0.1~1.1	227	49

Notes: HHTP: triphenylene-2,3,6,7,10,11-hexaol; CC: carbon cloth; H_3BTC: 1,3,5-benzene tricarboxylic acid; GCE: glassy carbon electrode; LDHs = layered double hydroxides; HLDH: hollow LDHs; HHNs = hydrophilic hierarchically-porous nanoflowers; TPA = terephthalic acid; SWCNT = single-walled carbon nanotubes; CuTiPNPs = copper-modified titanium phoshate nanoparticles; EG = exfoliated graphene; NT: nanotube; NSs = Nanosheets; GSPE = graphite screen-printed electrode; CPO-27-Ni^{II}: Ni_2(dihydroxyterephthalic acid); SiCNPs = silicon carbide nanoparticles; ENFM = electrospun-nanofibrous-membrane; ZIF-8 = zeolitic imidazolate framework 8; SPCE = screen-printed carbon electrodes; NF = nickel foam; MWCNTs-PB: multi-walled carbon nanotubes and Prussian blue; CoPO MA/NF = Cobalt phosphate microsheet arrays supported on Ni foam; NP = nano particles; Acb = acetylene black; mesoMOFs = mesoporous metal-organic frameworks; CNTs = carbon nanotubes.

Response time and anti-interference. Cu@Co-MOF/GCE exhibits a rapid current response of less than 7s to C_{Glu} change (Figure 6a). The anti-interference performance was evaluated by amperometric method. 0.1 mM Glu was added into 0.01 M NaOH and followed by the interferents of 0.01 mM D-Man, D-Fru, AA, DA, urea and UA, whose current reactions were recorded to evaluate the anti-interference of Cu@Co-MOF/GCE. As Glu is added, an obvious current response occurs; however, but the current responses are basically horizontal when D-Man, D-Fru, AA, DA, urea and UA are added (Figure 6b), showing a negligible influence of the interferents. Therefore, Cu@Co-MOF/GCE has high anti-interference for sensing Glu.

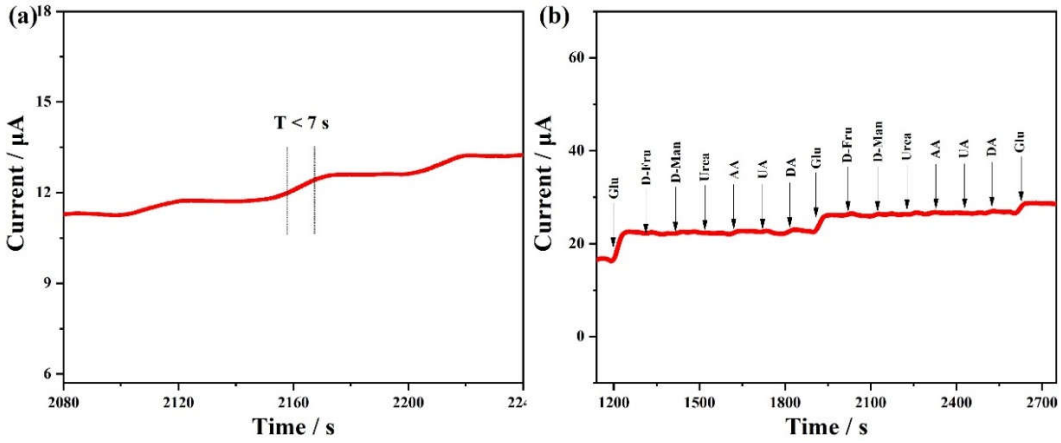

Figure 6. (a) The current response of Cu@Co-MOF/GCE to Glu; (b) the anti-interference of Cu@Co-MOF/GCE sensing 0.1 mM Glu with 0.01 mM D-Man, D-Fru, AA, DA, urea and UA as the interferents in 0.01 M NaOH at a working potential of +0.6 V.

Stability and repeatability. Stored at 4 ºC for 3-15 days, Cu@Co-MOF/GCE as non-enzymatic electrochemical sensor detects 1.0 mM Glu in 0.01 M NaOH every three days by amperometric method, whose current changes were recorded in Figure 7a. The current of the fresh Cu@Co-MOF/GCE is set as 100%. In the first three days, the current remains 96.50 %, then 85.78%, 77.06%, 72.39% and 69.25% for the following three-day sections. The current downward trend becomes slow. Even after the 15 days, Cu@Co-MOF/GCE still remains nearly 70% current response to Glu, indicating Cu@Co-MOF/GCE stays enough sensitivity and stability to Glu within 15 days. Five parallel measurements of sensing Glu were carried out with five groups of fresh Cu@Co-MOF/GCE sensors to evaluate the repeatability of Cu@Co-MOF/GCE (Figure 7b). The relative standard deviation (RSD) of the

Preprints (www.preprints.org) | NOT PEER-REVIEWED | Posted: 16 August 2022 doi:10.20944/preprints202208.0271.v1

five parallel measurements is 4.85 %, indicating the high repeatability of Cu@Co-MOF/GCE.

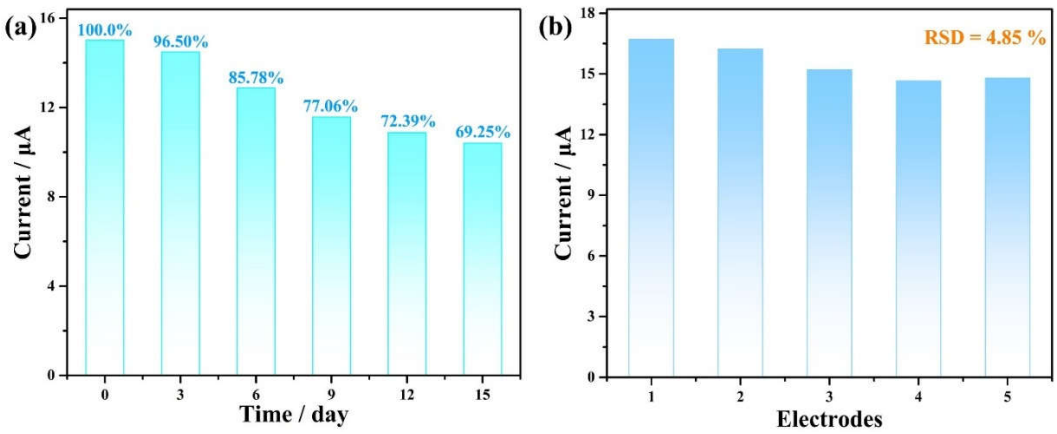

Figure 7. (a) The histogram of current *vs* storage time of Cu@Co-MOF/GCE sensing 1.0 mM Glu in 0.01 M NaOH with Cu@Co-MOF/GCE stored at 4 °C for 3-15 days; (b) the histogram of five parallel Glu detections by fresh Cu@Co-MOF/GCE sensing Glu.

3.4. Sensing Glu in human serum and orange juice

Standard addition method was used to evaluate the application performance of Cu@Co-MOF/GCE sensing Glu in human serum and orange juice. 50 μL human serum was diluted by 50 mL, 0.01 M NaOH, then 1.0 mM Glu followed to prepare 50, 100 and 200 μM Glu standard solutions. The current responses of each C_{Glu} were recorded for five times by CV method (Table 2). Through the linear equation of $j_{Cu@Co-MOF/GCE}\ (mA\ cm^{-2}) = 0.020C_{Glu}\ (\mu M) + 8.266$, the found C_{Glu}s were calculated as 50.01, 94.93 and 188.97 μM based on the found currents. The recoveries (defined as the found C_{Glu}/added C_{Glu}) were calculated as 100.02%, 94.93% and 94.49%. The RSDs (n = 5) range from 2.27% to 4.30%, all less than 5%.

The supernatant of minutemaid organic juice was obtained by a 8000-rpm centrifugation with for 5 min. 50 mL, 0.01 M NaOH diluted 50 μL extracted supernatants. Similar sensing Glu processes were carried out in a high-sugar orange juice. The found C_{Glu}s are 49.04, 93.27 and 189.54 μM, whose recoveries correspond to 98.08%, 93.27% and 94.77% with small RSDs ranging 1.61% to 3.08%. In total, the found C_{Glu}s in human serum and orange juice are close to the added C_{Glu}s, confirming non-enzymatic Glu sensor of Cu@Co-MOF/GCE can detect Glu with high accuracy and reliability. It suggests that Cu@Co-MOF/GCE can detect Glu accurately in the environments of rich endogenous biomolecules and high sugar content.

Table 2. The Glu sensing in human serum and orange juice by Cu@Co-MOF/GCE.

Samples	Added (μM)	Found ± SD (μM)	Recovery (%)	RSD
Serum	50	50.01 ± 2.15	100.02	4.30%
	100	94.93 ± 2.61	94.93	2.75%
	200	188.97 ± 4.23	194.49	2.24%
Orange juice	50	49.04 ± 1.60	98.08	1.61%
	100	93.27 ± 2.87	93.27	3.08%
	200	189.54± 4.46	94.77	2.35%

4. Conclusions

A cobalt metal-organic framework (Co-MOF), $[Co_3(BDC)_3(DMU)_2]$, was prepared via an ionothermal reaction, which features three 1D chains along the [110], [011] and *b*-

directions. The chains along the [110] and *b*-directions interconnect into a 2D [4,4] topological network, and finally shape a 2,6-connected $\{8^{12}.12^3\}\{8\}_3$ network by the connection of the [011] chains with the 2D layers. Co-MOF was further synthesized into a Cu@Co-MOF composite material through a sequential deposition-reduction process. Cu@Co-MOF/GCE composite electrode acts as a non-enzymatic electrochemical sensor to detect Glu in 0.01 M NaOH. Cu@Co-MOF/GCE shows excellent electrocatalytic activity for Glu detection. The chronoamperometric response of Cu@Co-MOF/GCE to C_{Glu} displays two linear relationships of $j = 0.020 \cdot C_{Glu} + 8.266$ (within 0.005-0.4 mM Glu) and $j = 0.012 \cdot C_{Glu} + 6.096$ (within 0.4-1.8 mM Glu) at a +0.6 V working potential. The sensitivities of Cu@Co-MOF/GCE are calculated as 282.89 and 113.15 μA mM^{-1} cm^{-2} respectively for the two C_{Glu} ranges. The detection limit is calculated as 1.6 μM at S/N = 3. The low detection limit and high sensitivities of Cu@Co-MOF/GCE to Glu detection are better than or compared with the other reported MOF-based non-enzymatic electrochemical Glu sensors. Furthermore, Cu@Co-MOF/GCE exhibits a rapid current response of less than 7s to C_{Glu} change, and a high anti-interference with 0.01 mM D-Man, D-Fru, AA, DA, urea and UA as the interferents. Within the storage time of 15 d, Cu@Co-MOF/GCE shows a gradually decreased current trend of 96.50 %, 85.78%, 77.06%, 72.39% and 69.25% for every three days' Glu electrochemical detection. The nearly 70% current response to Glu indicates an enough sensitivity and stability of Cu@Co-MOF/GCE within 15 days. Five parallel measurements with RSD of 4.85 % also demonstrate the high repeatability of Cu@Co-MOF/GCE. Glu detection were carried out in human serum and orange juice. All found C_{Glu}s are very close to those added C_{Glu}s with low RSDs and high recoveries. It indicates Cu@Co-MOF/GCE as a non-enzymatic Glu electrochemical sensor has a high accuracy and a reliability for Glu detection in real samples with rich endogenous biomolecules and sugars.

Supplementary Materials: Figure S1: The coordination modes of BDC^{2-} ligand in Co-MOF; Figure S2: The structure motif of the linear trinuclear $[Co_3(COO)_6(DMU)_2]$ SBU; Figure S3: $[Co_3(COO)_6(DMU)_2]$ SBUs connect BDC^{2-} ligands with O11/O12 (a), O21/O22 (b), and O31/O32 (c) into three 1D chains along the [110], *b*- and [011] directions respectively; Figure S4: The experimental XRD patterns of Co-MOF and Cu@Co-MOF compared to the simulated Co-MOF; Figure S5: FT-IR spectra of Co-MOF, Cu@Co-MOF and free H_2BDC ligand; Figure S6: TGA curve of Co-MOF; Figure S7: EDS of Co-MOF (a) and Cu@Co-MOF (b).

Author Contributions: Conceptualization, Ling Xu and Huan Jiao; Data curation, Zhen-Zhen Ma; Formal analysis, Zhen-Zhen Ma; Funding acquisition, Ling Xu and Huan Jiao; Investigation, Bing Liu and Zhen-Zhen Ma; Methodology, Ling Xu and Huan Jiao; Project administration, Ling Xu; Software, Bing Liu and Zhen-Zhen Ma; Validation, Bing Liu; Writing – original draft, Zhen-Zhen Ma; Writing – review & editing, Ling Xu.

Funding: The project was sponsored by Fundamental Research Funds for the Central Universities (GK202003032), Science and Technology program of Xi'an (201805027YD5CG11(3)), the Natural Science Foundation of Shaanxi province (2018JM2042).

Data Availability Statement: The original contributions presented in the study are included in the article. Further inquiries can be directed to the corresponding authors.

Conflicts of Interest: The authors declare no conflict of interest.

References

1. Wei, M.; Qiao, Y. X.; Zhao, H. T.; Liang, J.; Li, T. S.; Luo, Y. L.; Lu, S. Y.; Shi, X. F.; Lu, W. B.; Sun, X. P. Electrochemical non-enzymatic glucose sensors: recent progress and perspectives. *Chem. Commun*. **2020**, *56*, 14553-14569.
2. Wu, D.; Hu, D.; Chen, H.; Shi, G.; Fetahu, I. S.; Wu, F.; Rabidou, K.; Fang, R.; Tan, L.; Xu, S.; Liu, H.; Argueta, C.; Zhang, L.; Mao, F.; Yan, G.; Chen, J.; Dong, Z.; Lv, R.; Xu, Y.; Wang, M.; Ye, Y.; Zhang, S.; Duquette, D.; Geng, S.; Yin, C.; Lian, C. G.; Murphy, G. F.; Adler, G. K.; Garg, R.; Lynch, L.; Yang, P.; Li, Y.; Lan, F.; Fan, J.; Shi, Y.; Shi, Y. G. Glucose-regulated phosphorylation of TET2 by AMPK reveals a pathway linking diabetes to cancer. *Nature* **2018**, *559*, 637-641.

3. Puttananjegowda, K.; Takshi, A.; Thomas, S. Silicon carbide nanoparticles electrospun nanofibrous enzymatic glucose sensor. *Biosens. Bioelectron.* **2021**, *186*, 113285.
4. Wu, M.; Zhang, Y.; Liu, Q.; Huang, H.; Wang, X.; Shi, Z.; Li, Y.; Liu, S.; Xue, L.; Lei, Y. A smart hydrogel system for visual detection of glucose. *Biosens. Bioelectron.* **2019**, *142*, 111547.
5. Teymourian, H.; Barfidokht, A.; Wang, J. Electrochemical glucose sensors in diabetes management: an updated review (2010–2020). *Chem. Soc. Rev*. **2020**, *49*, 7671-7709.
6. Heller, A.; Feldman, B. Electrochemical Glucose Sensors and Their Applications in Diabetes Management. *Chem. Rev*. **2008**, *108*, 2482-2505.
7. Du, J.; Li, F.; Sun, L. Metal–organic frameworks and their derivatives as electrocatalysts for the oxygen evolution reaction. *Chem. Soc. Rev*. **2021**, *50*, 2663-2695.
8. Dong, Q.; Ryu, H.; Lei, Y. Metal oxide based non-enzymatic electrochemical sensors for glucose detection. *Electrochim. Acta* **2021**, *370*, 137744.
9. Rahmawati, I.; Einaga, Y.; Ivandini, T. A.; Fiorani, A. Enzymatic biosensors with electrochemiluminescence transduction. *ChemElectroChem.* **2022**, *9*, e202200175.
10. Khor, S. M.; Choi, J.; Won, P.; Ko, S. H. Challenges and strategies in developing an enzymatic wearable sweat glucose biosensor as a practical point-of-care monitoring tool for type II Diabetes. *Nanomaterials-Basel* **2022**, *12*, 221.
11. Osuna, V.; Vega-Rios, A.; Zaragoza-Contreras, E. A.; Estrada-Moreno, I. A. Dominguez, R. B. Progress of polyaniline glucose sensors for diabetes mellitus management utilizing enzymatic and non-enzymatic detection. *Biosensors-Basel* **2022**, *12*, 137.
12. Huang, W.; Huang, S. M.; Chen, G. S.; Ouyang, G. F. Biocatalytic metal-organic frameworks: promising materials for biosensing. *ChemBioChem*. **2022**, *23*, 202100567.
13. Chen, J. E.; Yang, Z. J.; Koh, H. U.; Shen, J.; Cai, Y. C.; Yamauchi, Y. Yeh, L. H.; Tung, V.; Wu, K. C. W. Current progress and scalable approach toward the synthesis of 2D metal-organic frameworks. *Adv. Mater. Inferfaces* **2022**, *9*, 2102560.
14. Li, N.; Xu, J.; Feng, R.; Hu, T. L.; Bu, X. H. Governing metal–organic frameworks towards high stability. *Chem. Commun*. **2016**, *52*, 8501-8513.
15. Xie, L. S.; Skorupskii, G.; Dincă, M. Electrically conductive metal–organic frameworks. *Chem. Rev.* **2020**, *120*, 8536–8580.
16. Adeel, M.; Asif, K.; Rahman, M. M.; Daniele, S.; Canzonieri, V.; Rizzolio, F. Glucose detection devices and methods based on metal–organic frameworks and related materials. *Adv. Funct. Mater.* **2021**, *31*, 2106023.
17. Shi, L. B.; Zhu, X.; Liu, T. T.; Zhao, H. L.; Lan, M. B. Encapsulating Cu nanoparticles into metal-organic frameworks for nonenzymatic glucose sensing. *Sens. Actuators B Chem*. **2016**, *227*, 583-590.
18. Zheng, L.; Liu, Y.; Zhang, C. A sample-to-answer, wearable cloth-based electrochemical sensor (WCECS) for point-of-care detection of glucose in sweat. *Sens. Actuators B Chem*. **2021**, *343*, 130131.
19. Ataei Kachouei, M.; Shahrokhian, S.; Ezzati, M. Bimetallic CoZn-MOFs easily derived from CoZn-LDHs, as a suitable platform in fabrication of a non-enzymatic electrochemical sensor for detecting glucose in human fluids. *Sens. Actuators B Chem*. **2021**, *344*, 130254.
20. Shang, N. Z.; Gao, S. T.; Zhou, X.; Feng, C.; Wang, Z.; Wang, C. Palladium nanoparticles encapsulated inside the pores of a metal–organic framework as a highly active catalyst for carbon–carbon cross-coupling. *RSC Adv.* **2014**, *4*, 54487-54493.
21. Deacon, G. B.; Phillips, R. J. Relationships between the carbon-oxygen stretching frequencies of carboxylato complexes and the type of carboxylate coordination. *Coord. Chem. Rev.* **1980**, *33*, 227-250.
22. Wei, Z.; Zhang, Z. H.; Wang, M. M.; Xu, L.; Liu, B.; Jiao, H. Combination effect of ligands and ionic liquid components on the structure and properties of manganese metal–organic frameworks. *CrystEngComm*. **2017**, *19*, 5402-5411.
23. Gross, P.; Höppe, H. A. Unravelling the urea-route to boron nitride: synthesis and characterization of the crucial reaction intermediate ammonium bis(biureto)borate. *Chem. Mater.* **2019**, *31*, 8052–8061.

24. Xue, R.; Guo, H.; Yue, L. G.; Wang, T.; Wang, M. Y.; Li, Q.; Liu, H.; Yang, W. Preparation and energy storage application of a long-life and high rate performance pseudocapacitive COF material linked with –NH– bonds. *New J. Chem.* **2018**, *42*, 13726-13731.
25. Zhang, J. H.; Zhou, T.; Wen, L.; Zhang, A. M. Fabricating metallic circuit patterns on polymer substrates through laser and selective metallization. *ACS Appl. Mater. Interfaces* **2016**, *8*, 33999–34007.
26. Zhang, J. H.; Zhou, T.; Wen, L. Selective Metallization Induced by Laser Activation: Fabricating metallized patterns on polymer via metal oxide composite. *ACS Appl. Mater. Interfaces* **2017**, *9*, 8996–9005.
27. Shao, Y. Y.; Gao, Y.; Yue, Q. Y.; Kong, W. J.; Gao, B. Y.; Wang, W. G.; Jiang, W. Q. Degradation of chlortetracycline with simultaneous removal of copper (II) from aqueous solution using wheat straw-supported nanoscale zero-valent iron. *Chem. Eng. J.* **2020**, *379*, 122384.
28. Xu, Z. H.; Wang, Q. Z.; Hui, Z. S.; Zhao, S.; Zhao, Y. J.; Wang, L. Carbon cloth-supported nanorod-like conductive Ni/Co bimetal MOF: A stable and high-performance enzyme-free electrochemical sensor for determination of glucose in serum and beverage. *Food Chem.* **2021**, *349*, 129202.
29. Kong, X. Y.; Xia, B.; Xiao, Y. W.; Chen, H. H.; Li, H. F.; Chen, W. Z.; Wu, P.; Shen, Y.; Wu, J. S.; Li, S.; Huo, F. W.; Zhang, W. N.; Zheng, B. Regulation of cobalt–nickel LDHs' structure and components for optimizing the performance of an electrochemical sensor. *ACS Appl. Nano Mater.* **2019**, *2*, 6387-6396.
30. Zhu, Q. Z.; Hu, S. Y.; Zhang, L. Q.; Li, Y.; Carraro, C.; Maboudian, R.; Wei, W.; Liu, A. R.; Zhang, Y. J.; Liu, S. Q. Reconstructing hydrophobic ZIF-8 crystal into hydrophilic hierarchically-porous nanoflowers as catalyst carrier for nonenzymatic glucose sensing. *Sens. Actuators B Chem*. **2020**, *313*, 128031.
31. Wang, X. D.; Zheng, Y. Y.; Yuan, J. H.; Shen, J. F.; Hu, J. G.; Wang, A. J.; Wu, L. J.; Niu, L. Three-dimensional NiCo layered double hydroxide nanosheets array on carbon cloth, facile preparation and its application in highly sensitive enzymeless glucose detection. *Electrochim. Acta* **2017**, *224*, 628-635.
32. Wang, F.; Chen, X. Q.; Chen, L.; Yang, J. L.; Wang, Q. X. High-performance non-enzymatic glucose sensor by hierarchical flower-like nickel(II)-based MOF/carbon nanotubes composite. *Mater. Sci. Eng. C* **2019**, *96*, 41-50.
33. Sun, F. C.; Wang, S. T.; Wang, Y. Q.; Zhang, J. T.; Yu, X. P.; Zhou, Y.; Zhang, J. Synthesis of Ni-Co hydroxide nanosheets constructed hollow cubes for electrochemical glucose determination. *Sensors*, **2019**, *19*, 2938.
34. Martín-Yerga, D.; Carrasco-Rodríguez, J.; Fierro, J. L. G.; Alonso, F. J. G.; Costa-García, A. Copper-modified titanium phosphate nanoparticles as electrocatalyst for glucose detection, *Electrochim. Acta* **2017**, *229*, 102-111.
35. Liu, B. B.; Wang, X. Y.; Liu, H. Q.; Zhai, Y. Y.; Li, L.; Wen, H. R. 2D MOF with electrochemical exfoliated graphene for nonenzymatic glucose sensing: Central metal sites and oxidation potentials. *Anal. Chim. Acta* **2020**, *1122*, 9-19.
36. Shahrokhian, S.; Sanati, E. K.; Hosseini, H. Advanced on-site glucose sensing platform based on a new architecture of free-standing hollow Cu(OH)2 nanotubes decorated with CoNi-LDH nanosheets on graphite screen-printed electrode. *Nanoscale*. **2019**, *11*, 12655-12671.
37. Chen, J. L.; Yin, H. Y.; Zhou, J. L.; Wang, L.; Gong, J Y.; Ji, Z. G.; Nie, Q. L. Efficient nonenzymatic sensors based on Ni-MOF microspheres decorated with Au nanoparticles for glucose detection. *J. Electron. Mater.* **2020**, *49*, 4754-4763.
38. Lopa, N. S.; Rahman, M. M.; Ahmed, F.; Sutradhar, S. C.; Ryu, T.; Kim, W. A Ni-based redox-active metal-organic framework for sensitive and non-enzymatic detection of glucose. *J. Electroanal. Chem*. **2018**, *822*, 43-49.
39. Wei, H. G.; Xue, Q. Z.; Li, A.; Wan, T.; Huang, Y.; Cui, D. P.; Pan, D.; Dong, B. B.; Wei, R. B.; Naik, N.; Guo, Z. H. Dendritic core-shell copper-nickel alloy@metal oxide for efficient non-enzymatic glucose detection. *Sens. Actuators B Chem.* **2021**, *337*, 129687.
40. Li, W. W.; Wang, S. L. Y.; Zhang, L.; Cui, X. Q. Nanoporous gold induced vertically standing 2D NiCo bimetal-organic framework nanosheets for non-enzymatic glucose biosensing. *Sens. Actuators B Chem*. **2019**, *281*, 652-658.
41. Lu, M. X.; Deng, Y. J.; Li, Y. C.; Li, T. B.; Xu J.; Chen, S. W.; Wang, J. Y. Core-shell MOF@MOF composites for sensitive nonenzymatic glucose sensing in human serum. *Anal. Chim. Acta* **2020**, *1110*, 35-43.

42. Wang, X.; Wang, M. Z.; Feng, S. Y.; He, D. P.; Jiang, P. Controlled synthesis of flower-like cobalt phosphate microsheet arrays supported on Ni foam as a highly efficient 3D integrated anode for non-enzymatic glucose sensing. *Inorg. Chem. Front*. **2020**, *7*, 108-116.
43. Yang, N.; Guo, K. L.; Zhang, Y. W.; Xu, C. L. Engineering the valence state of ZIF-67 by Cu2O for efficient nonenzymatic glucose detection. *J. Mater. Chem. B* **2020**, *8*, 2856-2861.
44. Peng, X. R.; Wan, Y.; Wang, Y. Y.; Liu, T.; Zou, P.; Wang, X. X.; Zhao, Q. B.; Ding, F.; Rao, H. B. Flower-like Ni(II)-based metal-organic framework-decorated Ag nanoparticles: fabrication, characterization and electrochemical detection of glucose. *Electroanal.* **2019**, *31*, 2179-2186.
45. Arif, D.; Hussain, Z.; Sohail, M.; Liaqat, M. A.; Khan, M. A.; Noor, T. A non-enzymatic electrochemical sensor for glucose detection based on Ag@TiO2@metal-organic framework (ZIF-67) nanocomposite. *Front. Chem.* **2020**, *8*, 573510.
46. Wen, Y. Y.; Meng, W.; Li, C.; Dai, L.; He, Z. X.; Wang, L.; Li, M.; Zhu, J. Enhanced glucose sensing based on a novel composite CoII-MOF/Acb modified electrode. *Dalton Trans*. **2018**, *47*, 3872-3879.
47. He, J.; Yang, H.; Zhang, Y. Y.; Yu, J.; Miao, L. F.; Song, L. F.Y. H.; Wang, L. Smart nanocomposites of Cu-hemin metal-organic frameworks for electrochemical glucose biosensing. *Sci Rep*. **2016**, *6*, 36637.
48. Song, Y. H.; Shen, Y.; Gong, C. C.; Chen, J. Y.; Xu, M. L.; Wang, L. Y.; Wang, L. A novel glucose biosensor based on Tb@mesoporous metal-organic frameworks/carbon nanotube nanocomposites. *ChemElectroChem.* **2017**, *4*, 1457-1462.
49. Shi, L. B.; Li, Y. F.; Cai, X.; Zhao, H. L.; Lan, M. B. ZIF-67 derived cobalt-based nanomaterials for electrocatalysis and nonenzymatic detection of glucose: Difference between the calcination atmosphere of nitrogen and air. *J. Electroanal. Chem*. **2017**, *799*, 512–518.